J Mater Sci

Ceramics

Proteic sol–gel synthesis of Gd-doped ceria: a comprehensive structural, chemical, microstructural and electrical analysis

Allan J. M. Araújo[1,2,*], João P. F. Grilo[3], Francisco J. A. Loureiro[2], Laura I. V. Holz[2], Daniel A. Macedo[4], Duncan P. Fagg[2], and Carlos A. Paskocimas[1]

[1] *Materials Science and Engineering Postgraduate Program – PPGCEM, UFRN, Natal 59078-970, Brazil*
[2] *Mechanical Engineering Department, Centre for Mechanical Technology and Automation, University of Aveiro, 3810-193 Aveiro, Portugal*
[3] *Department of Materials and Ceramic Engineering, University of Aveiro, 3810-193 Aveiro, Portugal*
[4] *Materials Science and Engineering Postgraduate Program – PPCEM, UFPB, João Pessoa 58051-900, Brazil*

Received: 15 June 2020
Accepted: 26 August 2020

ABSTRACT

Gd-doped ceria ($Ce_{1-x}Gd_xO_{2-\delta}$; x = 0, 0.1 and 0.2) is one of the best ceramic electrolytes for application in solid oxide electrochemical devices. This work reports an innovative and environmentally friendly route known as "proteic sol–gel synthesis" using gelatin for their preparation. Materials are characterized via thermogravimetric analysis, X-ray diffractometry, scanning electron microscopy, *Raman* and X-ray photoelectron spectroscopies, and electrochemical impedance spectroscopy. The proposed method allows to produce pure phase nanosized powders at 400 °C that exhibit excellent sinterability at 1350 °C. Significant differences are found in the bulk at lower temperatures, with estimated defect association enthalpies of 0.45 and 0.56 eV for the compositions containing 10 and 20 mol% Gd, respectively, leading to an increased bulk conductivity in the first case. In contrast, identical grain boundary *Schottky* barrier height values of around 0.2 V are a possible result of the relatively low sintering temperature, decreasing the extent of the acceptor dopant segregation to the grain boundaries due to insufficient cation mobility. This leads to similar specific grain boundary characteristics in both doped compositions. Overall, this work provides a rational understanding of a novel route for the synthesis of CGO ceramics with competitive performance and decreased sintering temperature.

Handling Editor: N. Ravishankar.

Address correspondence to E-mail: allanmenezes@ufrn.edu.br

https://doi.org/10.1007/s10853-020-05173-6

Published online: 21 September 2020

GRAPHIC ABSTRACT

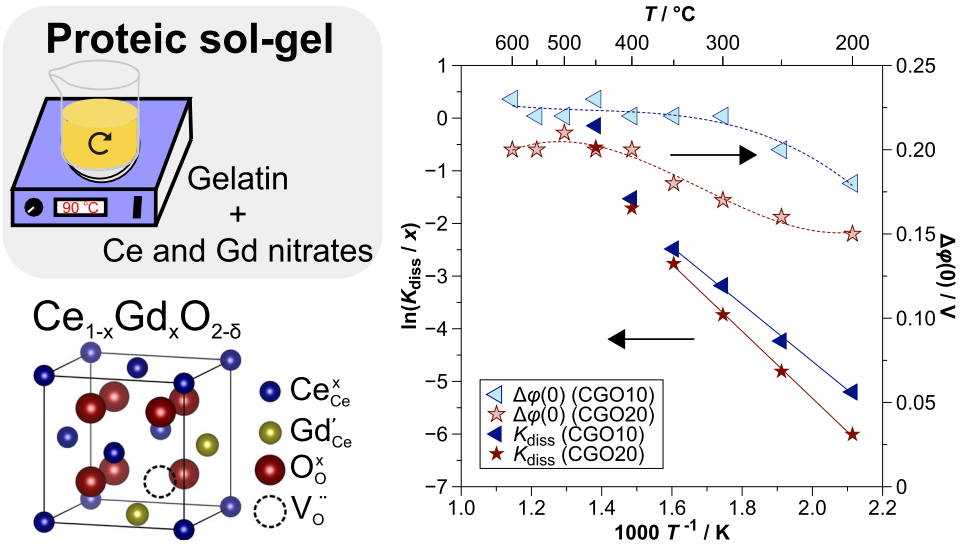

Introduction

Among all electrochemical energy conversion devices, solid oxide electrochemical systems, including solid oxide fuel cells (SOFCs) and solid oxide electrolyzer cells (SOECs), have received large attention due to their high efficiency and high flexibility for different fuels [1–3]. In this respect, Gd-doped ceria ($Ce_{1-x}Gd_xO_{2-\delta}$, CGO) has been studied as a promising electrolyte material due to its high oxide-ion conductivity at lower temperatures, when compared to the traditional yttria-stabilized zirconia (YSZ) [4, 5]. The partial substitution of Ce^{4+} by Gd^{3+} ions leads to the formation of oxygen vacancies, according to the following expression in *Kröger-Vink* notation, which is responsible for promoting oxide-ion conductivity:

$$Gd_2O_3 \longrightarrow CeO_2 2Gd'_{Ce} + 3O^X_O + V^{\cdot\cdot}_O \quad (1)$$

where Gd'_{Ce}, O^x_O and $V^{\cdot\cdot}_O$ correspond to a Gd^{3+} ion at the Ce^{4+} site, O^{2-} ion in the regular site of the oxygen sublattice lattice and an oxygen vacancy, respectively.

One of the main characteristics of the electrolyte is that it requires high densification to maximize its conductivity and to prevent the crossover of reactants during operation [6, 7]. However, the common solid-state route for materials preparation can include several milling and/or sieving steps, alternating with powder calcination, to obtain full reaction, thus, being susceptible to the addition of contaminants from abrasive materials during the milling process and phase impurities, which can influence the powder properties and compromise the reproducibility of each batch of the final powder. Moreover, the solid-state route usually requires very high sintering temperatures (1500–1600 °C) for sample densification, where cerium reduction (Ce^{4+} to Ce^{3+}) may occur, leading to microcracks on cooling that can damage the sample [6, 7].

Hence, in order to lower the sintering temperature, different researchers have studied the effect of low melting-point sintering additives, e.g., by the use of transition metal oxides (TMOs) [8]. In this respect, Fagg et al. [9] studied the effect of small additions of cobalt, iron and copper in the sinterability of CGO20, showing that a very low TMO content (2 mol%) could dramatically decrease the sintering temperature (897–1097 °C) and obtain highly dense CGO materials (95–99% relative density). Nonetheless, these TMOs were shown to lead to increases in the minor electronic conductivity of these materials in oxidizing atmospheres, due to segregation of these additives to the grain boundary [10]. Therefore,

although the addition of sintering additives can contribute to the sinterability of CGO, high electronic conductivity may arise due to enrichment of the grain boundaries of the material with the variable-valence cations diffused during the sintering step [9]. This factor may limit the applicability of the materials to be used as an electrolyte, due to potential internal electronic leakage of the electrochemical device [11].

In contrast, the formation of nanocrystalline powders can promote better sinterability at low temperatures to attain an adequate density without these drawbacks. In this respect, soft chemical syntheses are interesting alternative routes to obtain highly reactive powders and, subsequently, to lower the sintering temperature [12]. In line with this goal, a new synthesis route has been developed using commercial flavorless gelatin as an environmentally friendly and low-cost precursor, known as proteic sol–gel synthesis, being a "modified *Pechini* method" [13, 14]. The original *Pechini* method uses hydroxycarboxylic acids, such as citric acid, to form polybasic acid chelates, and a polyhydroxy alcohol, e.g., ethylene glycol, for a polyesterification reaction, resulting in a polymeric resin [15]. In contrast, the gelatin in the current proteic sol–gel route acts as a chelating agent for cations in solution (like citric acid) and as a polyhydroxy alcohol in a standard esterification process (like ethylene glycol) [13, 16].

In comparison to the traditional *Pechini* method, the proteic sol–gel method stands out by its low cost and for being a facile route, using only gelatin instead of citric acid and ethylene glycol. Gelatin is ~ 90% cheaper than the mixture citric acid + ethylene glycol (weight ratio of 60:40 for citric acid:ethylene glycol) often used in previous *Pechini*-related works [8, 17–19], considering the weight ratio of gelatin to citric acid + ethylene glycol of 1:1. This method has already been successfully used to synthesize several other materials for energy conversion and storage-related applications [13, 14, 16, 20–23].

Nevertheless, and despite being one the best intermediate temperature electrolytes, to the best of our knowledge, no reports currently exist on the use of the proteic sol–gel route for the preparation of Gd-doped ceria compounds. Moreover, although the Gd_2O_3-CeO_2 system has been reported by several authors, few works provide a comprehensive microstructural and electrical analysis of 0, 10 and 20 mol% Gd_2O_3-doped CeO_2, formed by such low temperature, soft chemical preparation routes. Hence, in this work, we synthesized $Ce_{1-x}Gd_xO_{2-\delta}$ (x = 0, 0.1 and 0.2) nanoparticles by the proteic sol–gel route for intermediate temperature electrochemical applications. The synthesized materials are fully characterized by their structural, chemical, microstructural and electrical properties.

Materials and methods

Powder synthesis

Powders with nominal composition $Ce_{1-x}Gd_xO_{2-\delta}$ (x = 0, 0.1 and 0.2, named as CeO_2, CGO10 and CGO20), respectively, were prepared by the proteic sol–gel method with gelatin as polymerizing agent, using cerium(III) nitrate hexahydrate ($Ce(NO_3)_3{\cdot}6H_2O$, 99%, Sigma-Aldrich) and gadolinium(III) nitrate hexahydrate ($Gd(NO_3)_3{\cdot}6H_2O$, 99.9%, Sigma-Aldrich) as starting materials. First, a flavorless gelatin was dissolved in distilled water at around 60–70 °C. After complete dissolution, Ce nitrate was added to obtain the precursor resin of CeO_2; while, in the case of Gd-doped samples, Ce and Gd nitrates were simultaneously added (in stoichiometric amounts) into two different solutions to obtain the precursor resins of CGO10 and CGO20. After addition of all the nitrates, the temperature was increased to 90 °C until complete dryness. Finally, the resins were heat treated at 300 °C and subsequently calcined at 400 °C.

Powder characterization

Thermogravimetric analysis was performed using a Shimadzu TGA 60-H thermogravimetric analyzer under air atmosphere from room temperature to 900 °C, with a heating rate of 10 °C min^{-1}. Structural characterization was carried out by X-ray diffractometry in the range of 10–80° (2θ, with a scanning speed of 1° min^{-1} (continuous scan mode), operating with a voltage of 40 kV, current of 30 mA and using Cu Kα radiation source (Shimadzu, model XRD 7000). *Rietveld* refinement of the XRD data was performed using MAUD software (Materials Analysis Using Diffraction—version 2.93). The prepared ceria powder was characterized by using field-emission scanning electron microscopy (FESEM, Carl Zeiss, Supra 35-VP Model).

Raman spectroscopy measurements were also conducted at room temperature using a laser with an

excitation wavelength of 532 nm (LabRAM HR Evolution, HORIBA). Laser power was kept at 1 mW with an acquisition time of 10 s and 20 accumulations. Structural characterization of powders was also performed by X-ray photoelectron spectroscopy (XPS). XPS spectrums were acquired in an Ultra High Vacuum (UHV) system with a base pressure of 2×10^{-10} mbar. The system is equipped with a hemispherical electron energy analyzer (SPECS Phoibos 150), a delay-line detector and a monochromatic AlKα (1486.74 eV) X-ray source. High-resolution spectra were recorded at a normal emission take-off angle and with a pass-energy of 20 eV, which provides an overall instrumental peak broadening of 0.5 eV. The C 1s binding energy referencing method was used, and all spectra were corrected with reference to adventitious carbon at 285 eV for charge control, according to the ISO 19,318:2004 and ASTM E1523-15 guides [24, 25]. In order to fit the XPS spectra, *XPSPeak* 4.1 software was used. Accordingly, the number of peaks, the full width at half maximum (FWHM), peaks positions and shapes (% of Lorentzian and Gaussian functions used) were optimized aiming to obtain the best fit. For Ce^{3+}/Ce^{4+} ratio calculations, the peak area of each region was divided by the photoionization cross-section factor of the respective element, accordingly [26].

Densification and microstructural characterization

Pellets were prepared by uniaxial pressing at 200 MPa and sintered in air at both 1300 and 1350 °C for 4 h using a heating rate of 3 °C min^{-1}. The microstructural characterization of the sintered samples was carried out by a scanning electron microscope (SEM, Hitachi SU-70) coupled with an energy dispersive X-ray detector (EDS, Bruker Quantax 400). The average grain size was determined by measuring grains from the sample surfaces using *ImageJ* software. Apparent densities of the sintered samples were determined by the Archimedes' principle in distilled water, and the relative densities were calculated from the ratio between the apparent densities and the theoretical densities calculated from the XRD lattice parameter data.

Electrical characterization

The electrical characterization of undoped and doped ceria samples was performed by impedance spectroscopy (Hewlett Packard 4284A LCR Meter) in air between 200 and 600 °C. Impedance spectroscopy measurements were made in a frequency range between 20 Hz and 1 MHz using 0.5 V signal amplitude. The results were analyzed using *ZView*® software (Scribner Associates, Inc., version 3.0).

Results and discussion

Powder characterization

Figure 1 shows the thermogravimetric analysis of the CeO_2 precursor resin obtained from the synthesized gel after drying at 100 °C overnight (solid line), the respective first derivative (circles) and the CeO_2 resin heat-treated at 300 °C (short dash line). As observed in the resin curve and its derivative, the first stage corresponds to complete dehydration, nitrate decomposition, and some initial decomposition of organic material. The second stage (up to 350 °C) is related to the complete elimination of organic matter from the gelatin (with the release of CO, CO_2 and other gases). These results are in good agreement to those previously reported by Braga et al. [27]. From the CeO_2 powder heat-treated at 300 °C, no significant weight loss was observed. It is important to emphasize from these results that the total weight loss using gelatin as polymerizing agent to obtain ceria-based material occurred below 400 °C. In contrast, the traditional *Pechini* method (using citric acid and polyethylene glycol) requires much higher

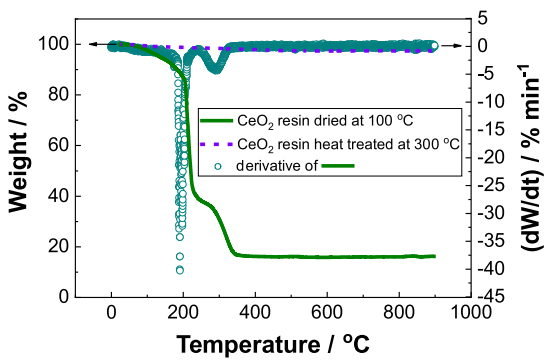

Figure 1 TG profiles of gelatin and cerium nitrate solution dried at 100 °C, CeO_2 powder after heat treatment at 300 °C and DTG for the dried solution.

temperatures to remove the organic contents, as seen in the work of Lima et al. (total weight loss occurred at ~ 600 °C) [8].

The synthesized materials were structurally characterized by XRD, after calcination at 400 °C, as shown in Fig. 2. All XRD patterns show a single-phase fluorite-type structure (CaF_2, space group symmetry: $Fm\bar{3}m$—number 225), indicating the complete dissolution of Gd cations into the CeO_2 lattice in both CGO10 and CGO20 samples (Fig. 2a). All the peaks were indexed according to the ICSD collection codes 88,759, 28,795 and 182,976 for CeO_2, CGO10 and CGO20, respectively. Figure 2 (b) depicts the magnification of the most intense peak (111), clearly showing a shift toward lower 2θ angles with increasing Gd content, corresponding to an increase in the lattice parameter (Table 1). This phenomenon can be explained by the substitution of the smaller cerium cations $\left(r_{Ce^{4+}}^{(VIII)} = 97pm\right)$ [28] by the larger gadolinium cations $\left(r_{Gd^{3+}}^{(VIII)} = 105pm\right)$ [28], promoting a slight expansion of the ceria fluorite structure. In addition, the crystallite size calculated for the samples by the *Rietveld* refinement (11–22 nm, Table 1) is in agreement with that observed from the FESEM image of the calcined CeO_2 nanoparticles depicted in Supplementary Fig. S1.

Structural characterization was also performed by *Raman* spectroscopy at room temperature, as shown in Fig. 3a. All three compositions show a *Raman* active mode located at around 460 cm^{-1}, which is attributed to the F_{2g} symmetric vibration mode of the

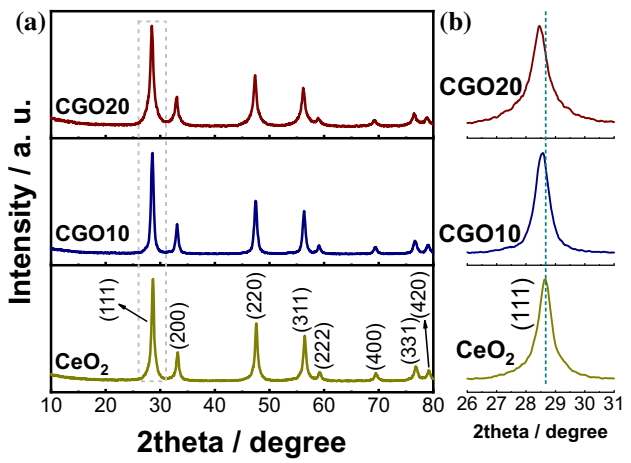

Figure 2 **a** XRD patterns and **b** magnification of the (111) peak region (2θ = 26–31°) of the samples calcined at 400 °C.

Ce–O bond in eightfold coordination [30]. In the CGO20 sample, the F_{2g} vibration can be noted to shift to lower wavenumbers, possibly due to structural defects caused by the extensive amount of Gd doping in this case. The *Raman* active mode at 600 cm^{-1} may be due to oxygen deficiency, which is attributed to the intrinsic oxygen vacancies generated from the presence of Ce^{3+} ions (see later in XPS results). The *Raman* mode centered at 550 cm^{-1} (CGO10 and CGO20 samples) is ascribed to structural defects (expansion of ceria lattice) or extrinsic oxygen vacancies in the ceria lattice created to compensate the valence imbalance induced by the Gd^{3+} replacing Ce^{4+} [31]. It is important to mention that the intensity of this *Raman* band progressively increases with the Gd doping content due to the increased oxygen vacancies concentration generated by the doping effect, Eq. (1). The absence of a mode at ~ 350 cm^{-1} proves that isolated amounts of the Gd_2O_3 phase were not obtained in the CGO10 and CGO20 samples [32], in good agreement with the pure fluorite-type phases indicated in the XRD results shown previously.

X-ray photoelectron spectra of the CeO_2 and CGO20 powders are shown in Fig. 3b–f. The overview spectra are shown in Fig. 3b, and the high-resolution spectra of the core levels of Ce 3d and O 1s were deconvoluted, as seen in Fig. 3c–f. Ce 3d scan shows spectra with ten deconvoluted peaks (Fig. 3c, d). The relative amount of Ce^{3+} was calculated as follows:

$$\frac{[Ce^{3+}]}{[Ce^{3+}] + [Ce^{4+}]} = \frac{\text{area } (v_0, v', u_0, u')}{\text{total area}} \quad (2)$$

where photoionization cross-sections were taken into account. It was found that the CeO_2 sample presents 13% of Ce^{3+}, whereas CGO20 presents 24% of Ce^{3+}. The higher Ce^{3+} content in the Gd-doped ceria sample may be due to the more facile reduction of ceria, as previously reported, enhanced by the synergistic interaction between gadolinium and cerium [31]. The O 1s spectra were fitted with two main peaks, as shown in Fig. 3e, f, corresponding to oxygen in the lattice, often associated with metal–oxygen bonds (O_L, 529.22 and 526.86 eV), and defective sites with low oxygen coordination—vacancies (O_V, 532.02 and 529.67), as reported in a previous work [33]. CeO_2 shows a O_V/O_L ratio of 0.08, against 0.46 for CGO20. Therefore, the XPS results confirm that

Table 1 Crystallite sizes, lattice parameters ($a = b = c$) and *Rietveld* agreement indexes for the ceria-based compositions]

Sample	Crystallite size (nm)	Lattice parameter (Å)	R_{wp} (%)	R_{exp} (%)	χ^2
CeO_2	16.6	5.4164(5)	17.47	13.77	1.27
CGO10	22.4	5.4204(4)	15.80	13.41	1.18
CGO20	10.8	5.4279(9)	17.02	13.47	1.26

The chi-square (χ^2) values obtained (1.18–1.27) evidence the good quality of the fit between the calculated and the experimental patterns [29

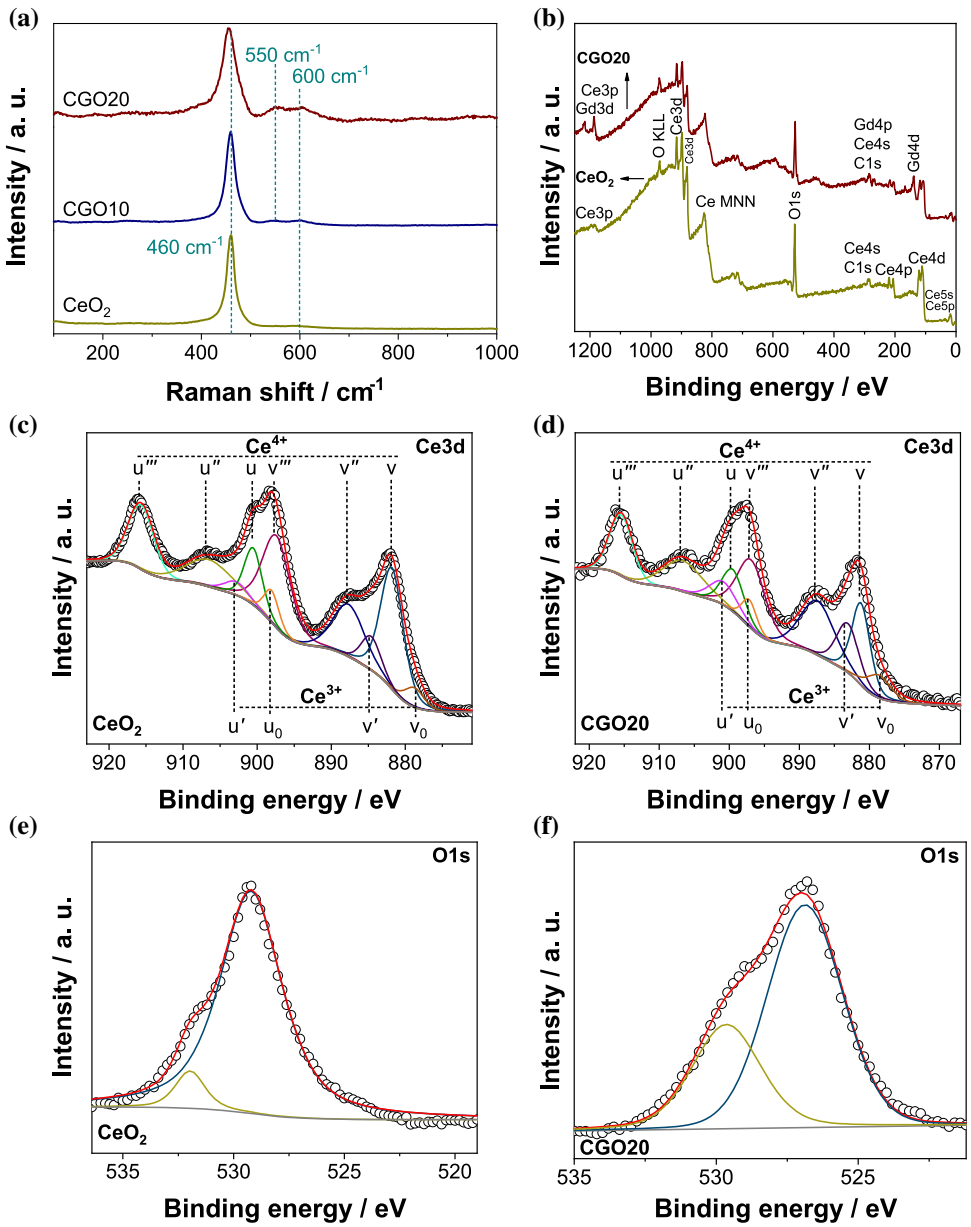

Figure 3 **a** Room-temperature *Raman* spectra of CeO_2, CGO10 and CGO20. XPS spectra of CeO_2 and CGO20: **b** Overview, **c**, **d** Ce3d for CeO_2 and CGO20, respectively, and **e**, **f** O 1s for CeO_2 and CGO20, respectively.

CGO20 exhibits higher oxygen vacancy content, in agreement with its more extensive Gd doping level.

The *Raman* and XPS results support the XRD discussions and reinforce that the proteic sol–gel route can successfully form the $Ce_{1-x}Gd_xO_{2-\delta}$ ($x = 0$, 0.1 and 0.2) solid solutions, even at the very low calcination temperature of 400 °C.

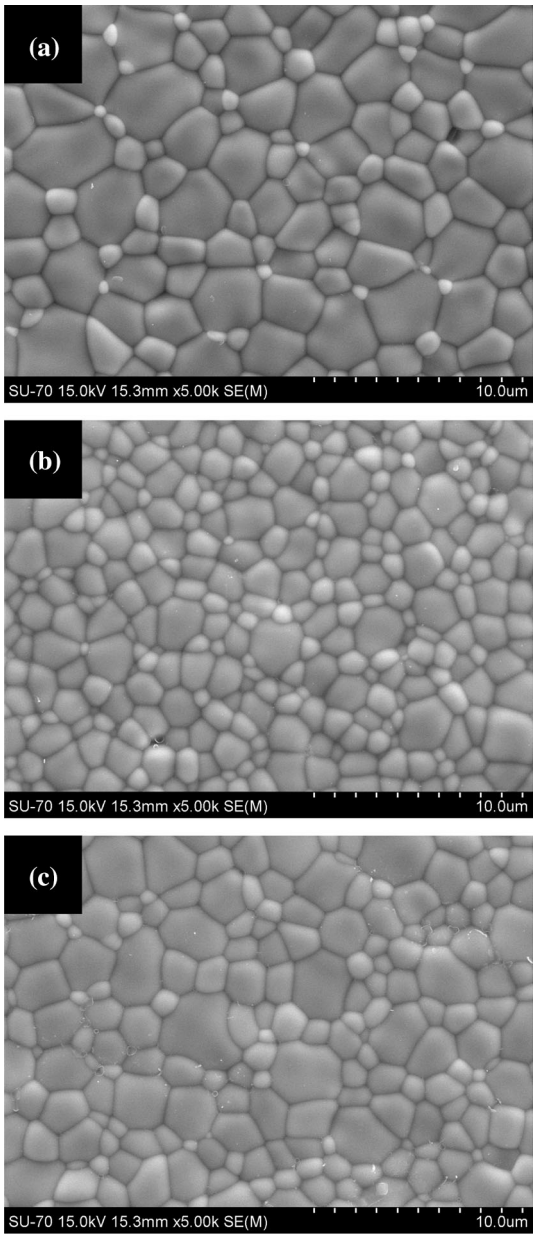

Figure 4 SEM images of the undoped and Gd-doped ceria pellets sintered at 1350 °C: **a** CeO_2, **b** CGO10 and **c** CGO20.

Densification and microstructure

Figure 4 shows the microstructures of the pellets sintered at 1350 °C, obtained for CeO_2, CGO10 and CGO20 samples. All samples denote highly dense microstructures, with relative densities varying between 96 and 98%, showing the excellent sinterability of powders prepared by the proteic sol–gel route in comparison to other routes in the literature, where significantly higher sintering temperatures typically have to be used (Table 2). Table 2, therefore, underscores the great advantage of the current synthesis method over that of traditional synthesis routes. In addition, the EDS maps found in Supplementary Fig. S2 reveal that Ce and Gd elements are homogeneously distributed in the CGO10 and CGO20 samples after sintering at 1350 °C, with no evidence of localized Gd spots. In addition, the quantification results show that the values of each element are close to the nominal compositions (CGO10 and CGO20), in good accordance with the complete solid-solution formation between CeO_2–Gd_2O_3.

Another important feature of the sintered electrolytes is the slight decrease in the grain size of the doped compositions, in comparison to that of pure CeO_2 (Table 3). This feature is likely to be related to the formation of an enriched layer of Gd'_{Ce} species at the adjacent space-charge layers of the CGO samples, with a steep gradient between bulk and intergranular interfaces, giving a strong solute drag to the grain boundary mobility and an effective retardation of grain growth, as previously reported in similar materials [34, 35].

Electrical properties

Impedance spectra obtained for the samples sintered at 1350 °C, are represented in Fig. 5 for different temperatures measured in air atmosphere (p_{O2} = 0.21 atm). Distinct contributions can be seen depending on sample composition and measuring temperature. At low temperatures (200 °C, Fig. 5a), only the bulk contribution (CeO_2) or bulk plus grain boundary contributions (CGO10 and CG20) are observed. As the temperature increases ($T \geq 300$ °C), information on the high and intermediate frequency semicircles starts to not be visible in the measured frequency range of the experiment, while a low-frequency electrode tail starts to be observed [10]. Hence, three equivalent circuits have been used to fit the impedance data, based on series combinations of parallel R (resistors) and CPE (constant phase elements) units, as depicted in Fig. 5. The calculated capacitance for the bulk response is $\sim 10^{-11}$ F cm^{-1}, and for the grain boundary (g.b.) is in the range 10^{-9}–10^{-8} F cm^{-1}, in agreement with previous works [47].

Figure 6 shows the typical temperature dependence of the total conductivity in the temperature range of 200–600 °C (note, for the CeO_2 sample, only the range 300–600 °C is presented due to the inability

Table 2 Comparison of relative densities at different sintering temperatures of ceria-based samples prepared by different routes

Ceria-based sample	Method	Relative density					Reference
		At 1300 °C (%)	At 1350 °C (%)	At 1400 °C (%)	At 1450 °C (%)	At 1500 °C (%)	
CeO_2	Proteic sol–gel	92.8	97.6	–	–	–	This study
$Ce_{0.9}Gd_{0.1}O_{1.95}$	Proteic sol–gel	94.1	96.8	–	–	–	This study
$Ce_{0.8}Gd_{0.2}O_{1.9}$	Proteic sol–gel	90.9	96.4	–	–	–	This study
$Ce_{0.8}Sm_{0.2}O_{1.9}$	Oxalate coprecipitation	–	96.6	–	–	–	[36]
$Ce_{0.8}Sm_{0.2}O_{1.9}$	Glycine-nitrate	–	96.4	–	–	–	[36]
$Ce_{0.9}Gd_{0.1}O_{1.95}$	Glycine-nitrate	–	95	–	97	–	[37]
$Ce_{0.9}Gd_{0.1}O_{1.95}$	*Pechini*	90	–	98	–	–	[38]
$Ce_{0.8}Sm_{0.2}O_{1.9}$	Glycine-nitrate	90.7	–	~ 97.5	–	~ 99	[39]
$Ce_{0.9}Gd_{0.1}O_{1.95}$	Commercial powder, Praxair	84.2	–	97.5	–	–	[40]
$Ce_{0.9}Gd_{0.1}O_{1.95}$	Gelcasting	~ 82	~ 91	~ 94	~ 96	~ 97	[41]
$Ce_{0.8}Gd_{0.2}O_{1.9}$	Microwave-assisted	–	–	93.9	–	–	[42]
Samarium-doped ceria	Oxalate coprecipitation	–	86.7	–	–	–	[43]
$Ce_{0.9}Gd_{0.1}O_{1.95}$	Oxalate coprecipitation	< 65	~ 81	~ 90	~ 93	~ 95	[41]
$Ce_{0.9}Gd_{0.1}O_{1.95}$	Citrate complexation	–	–	–	93.9	–	[44]
$Ce_{0.9}Gd_{0.1}O_{1.95}$	*Pechini*	–	–	–	–	95	[8]
$Ce_{0.9}La_{0.1}O_{1.95}$	Coprecipitation	–	–	–	–	≥ 94	[45]
$Ce_{0.9}Gd_{0.1}O_{1.95}$	Solid-state reaction	–	~ 66.2	–	–	–	[46]

Table 3 Average grain size of the samples sintered at 1350 °C

Composition	Average grain size (μm)
CeO_2	2.134 (± 0.842)
CGO10	1.502 (± 0.437)
CGO20	1.831 (± 0.668)

to resolve the grain-boundary contribution at 200 and 250 °C, within the frequency range of the experiment). In general, the total conductivities of the doped compositions are significantly higher than that of pure ceria, due to a much higher oxygen vacancy concentration, and hence, oxide-ion conductivity (Eq. 1). Total conductivities and activation energies of the ceria-based samples are shown in Table 4. The Arrhenius law was used to retrieve activation energy values:

$$\sigma T = \sigma_0 \exp\left(-\frac{E_a}{RT}\right) \quad (3)$$

where σ is the electrical conductivity, σ_0 is a pre-exponential factor, E_a is the activation energy, R is the gas constant (8.314 J mol^{-1} K^{-1}) and T is the measuring temperature.

The activation energy values in Table 4 are in line with those of doped ceria compositions from the literature (0.98–1.21 eV) [48]. To understand this behavior in more depth, a detailed discussion of the doped systems will follow on the analysis of the individual behaviors of both bulk and grain boundary.

Bulk properties

Figure 7 depicts the temperature dependence of the bulk conductivity obtained for CGO10 and CGO20 samples in air, in the temperature range 200–600 °C. The bulk conductivity is observed to be higher in the case of the Gd-doped samples, in all cases, in agreement with the increased oxide-ion vacancy content ($V_O^{\cdot\cdot}$) on Gd doping, according to Eq. (1). However,

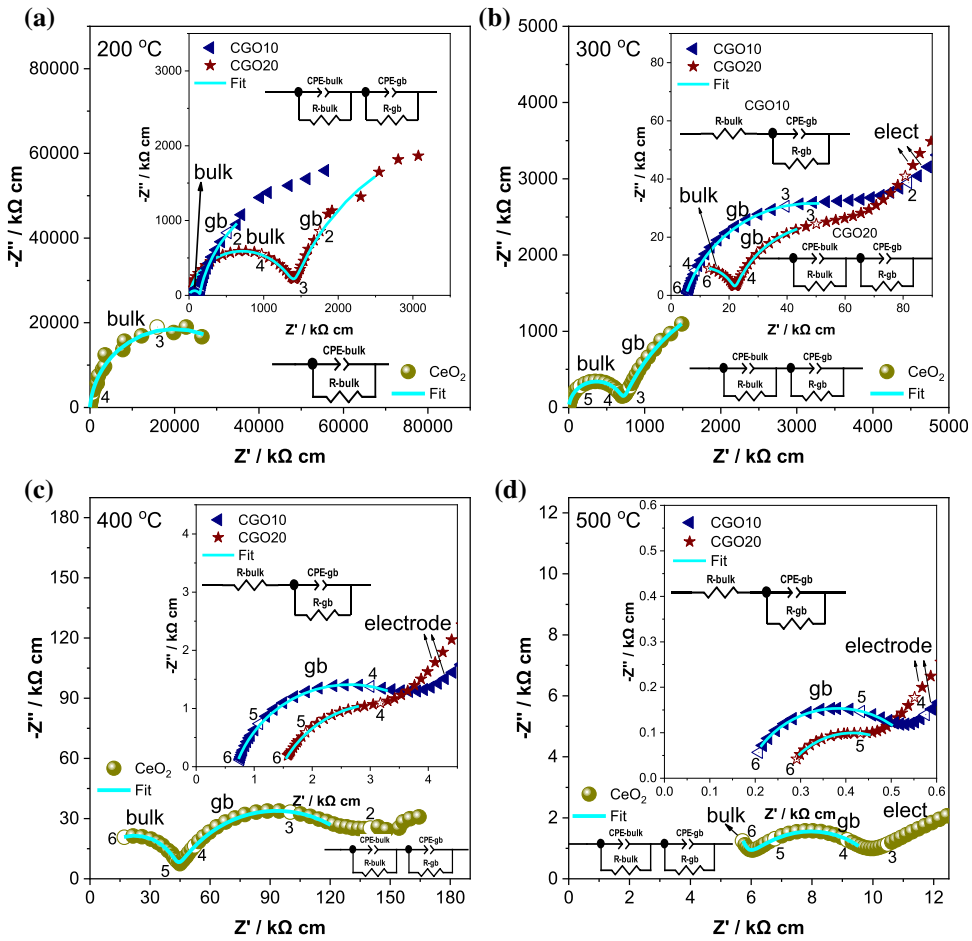

Figure 5 Impedance spectra of CeO_2, CGO10 and CGO20 electrolytes measured in air (p_{O2} = 0.21 atm) at different temperatures: **a** 200, **b** 300, **c** 400, and **d** 500 °C. Numbers close to data points indicate the log10 of frequency.

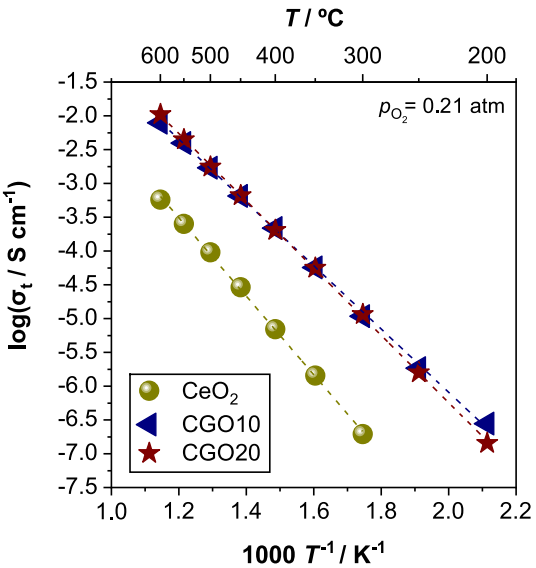

Figure 6 Arrhenius plots of the total conductivities for samples $Ce_{1-x}Gd_xO_{2-\delta}$ (x = 0, 0.1 and 0.2).

below 500 °C, a higher bulk conductivity in the case of CGO10 can be observed in comparison to that of

Table 4 Activation energy values of the total conductivity of the tested electrolytes

Sample	Activation energy (eV)
CeO_2	1.21
CGO10	0.98
CGO20	1.04

CGO20. This feature at low temperatures has been noted previously for these materials and attributed to the formation of defect associates $(Gd_{Ce} \cdot V_O)^{\cdot}$ with lower mobility [49]. This concept is supported by the measured activation energies. The bulk conductivity (σ_{bulk}) shows two linear segments: (i) at low temperature (200–500 °C) and (ii) at high temperature (500–600 °C). The low temperature case denotes a higher activation energy value in the range 0.8–1 V for both samples in comparison to that estimated at high temperature (0.50–0.56 eV) (Table 5), due to the presence of an additional association binding energy that results from the presence of defect associations

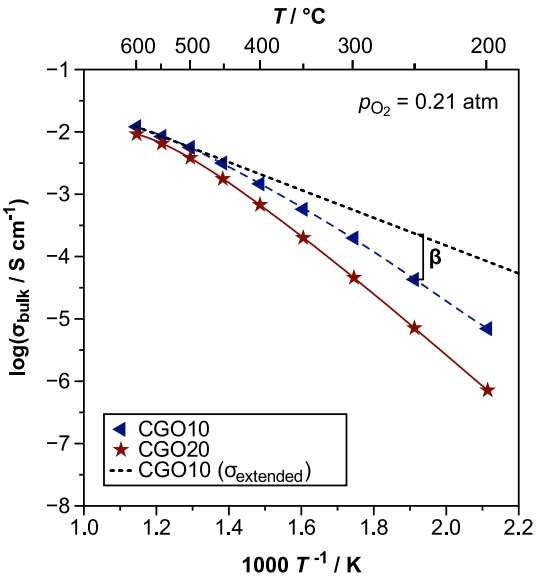

Figure 7 Temperature dependence of the bulk conductivities. Dashed line represents the extended conductivity ($\sigma_{extended}$) of the bulk using the activation energy obtained at high temperatures to determine the extent of the defect association (β).

[49]. As a result, the CGO10 sample exhibits a higher bulk conductivity than that of the CGO20 sample at low temperatures, due to its lower dopant content and lower concentration of defect associates [49]. On the other hand, at high temperatures, a negligible difference is observed between both samples due to the breaking of the defect associations (Eq. 6) and elimination of the association binding energy contribution to ionic migration. The analysis was further performed by separating the contribution from both free vacancies and defect associates, following a methodology developed earlier [50], and shown in Table 5.

The experimental σ_{bulk} was extrapolated to low temperature using high-temperature activation energy values, which is represented as $\sigma_{extended}$. The bulk conductivity is lowered by a factor β, assuming the following relationship (Fig. 7):

$$\sigma_{bulk} = \sigma_{extended} \times \beta \tag{4}$$

where β can also be considered as a measure of the extent of defect interactions, and, on neglecting changes in the mobility, it gives that

$$\beta = \frac{[V_O^{\cdot\cdot}]_{effective}}{[V_O^{\cdot\cdot}]_{nominal}} \tag{5}$$

which represents the ratio between the effective charge carrier ($[V_O^{\cdot\cdot}]_{effective}$) and the nominal vacancy ($[V_O^{\cdot\cdot}]_{nominal}$) concentrations, as depicted in Fig. 8a, on assuming dominance of $[V_O^{\cdot\cdot}]_{nominal}$ at high temperature. As observed in Fig. 8a, this ratio approaches unity at 500 °C as a result of the increase in the concentration of free oxide-ion vacancies with increasing temperature:

$$(Gd_{Ce} \cdot V_O)^{\cdot} = V_O^{\cdot\cdot} + Gd'_{Ce} \tag{6}$$

with an equilibrium constant for dissociation given by

$$K_{diss} = \frac{[V_O^{\cdot\cdot}]_{effective} \times [Gd'_{Ce}]}{[(Gd_{Ce} \cdot V_O)^{\cdot}]} \approx \frac{x}{2} \times \beta \times \frac{(1+\beta)}{1-\beta} \tag{7}$$

where the actual concentrations are expressed as a fraction of the total number of cation sites and x denotes the total content of Gd in the sample. Figure 8b depicts the K_{diss} estimated for both samples as a function of temperature, where a lower value is observed in the case of CGO20. Moreover, the temperature dependence of K_{diss} is observed to become linear at the lowest temperatures [50]. Hence, the enthalpies for association (ΔH_{ass} were estimated in this region, and correspond to the slope of the Arrhenius plots of conductivity (Table 5), assuming the following relationship

$$E_{a,bulk}(\sigma_{bulk}) = \Delta H_m + \Delta H_{ass} \tag{8}$$

where the enthalpy for migration (ΔH_m) was calculated from the activation energy obtained at high temperature. Earlier works have also ascribed the change in activation energy to the migration and association enthalpies [50, 51]. From Table 5, one can

Table 5 Activation energy for the bulk responses and estimates of migration and association enthalpies extracted from $\ln(\sigma T)$ vs. 1000 T^{-1} ($\Delta H_{ass\ (\sigma)}$) and $\ln(K_{diss})$ vs. 1000.T^{-1} ($\Delta H_{ass\ (K)}$) and the dielectric permittivity of the bulk

Composition	$E_{a\ (low)}$ (eV)	$E_{a\ (high)}$ (eV)	ΔH_m (eV)	$\Delta H_{ass\ (\sigma)}$ (eV)	$\Delta H_{ass\ (K)}$ (eV)	ε_r
CGO10	0.80	0.50	0.44	0.29	0.45	63
CGO20	0.98	0.56	0.49	0.42	0.56	68

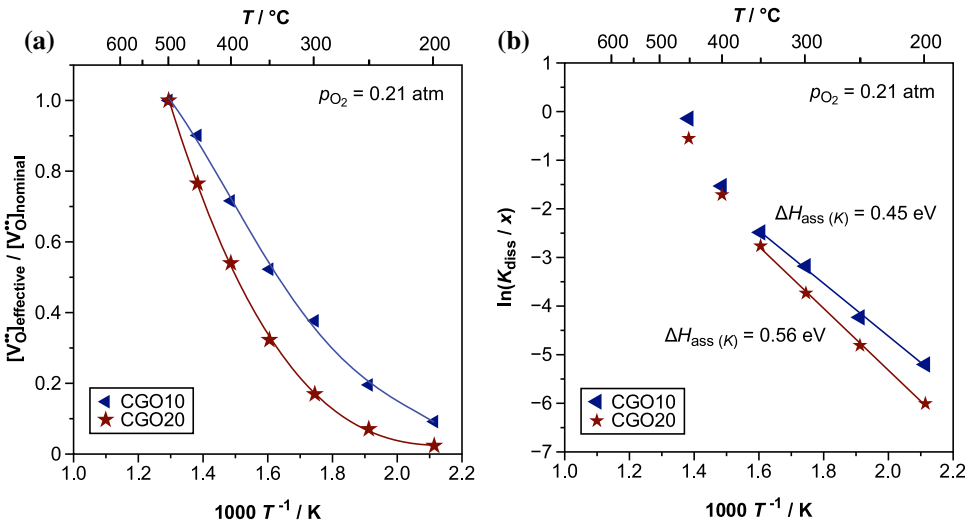

Figure 8 Temperature dependence of: **a** ratio between the effective charge carrier and the nominal vacancy concentration; **b** equilibrium constant for defect dissociation.

observe a slight increase in the enthalpy for migration in the case of CGO20 sample, as expected due to an increase of acceptor dopant concentration [50], whereas Fig. 8a highlights that the CGO20 sample suffers strongly from a depletion of mobile oxygen vacancies at low temperatures due to the presence of defect associates.

Grain boundary properties

The brick-layer model (BLM) was used to explain the intrinsic properties of the grain boundary. Thus, the specific grain boundary conductivity ($\sigma^*_{g.b.}$) was calculated using the following equation:

$$\sigma_{g.b}* = 2\pi f_{g.b} \cdot \varepsilon_0 \cdot \varepsilon_{r,g.b} \tag{9}$$

where $f_{g.b.}$ is the relaxation frequency that is given by

$$f_{g.b} = (2\pi \cdot R_{g.b} \cdot C_{g.b})^{-1} \tag{10}$$

And ε_0 is the permittivity of the vacuum, and $\varepsilon_{r,g.b.}$ is the dielectric permittivity of the grain boundary calculated from that of the bulk response ($\varepsilon_{r,g.b.} \approx \varepsilon_{r,bulk}$) (Table 5) [52, 53], $R_{g.b.}$ is the grain boundary resistance, and $C_{g.b.}$ is the grain boundary capacitance.

Figure 9 depicts the temperature dependence of both the $\sigma^*_{g.b.}$ and the relaxation $f_{g.b.}$ for CGO10 and CGO20, from which negligible differences can be observed between both samples. Hence, for a rational understanding of this behavior, the space charge properties at the grain boundary were analyzed in detail.

A space-charge model was employed to both CGO10 and CGO20 samples using a *Mott-Schottky* approximation that assumes a constant concentration of the acceptor dopant species (Gd'_{Ce}) in the space-charge layers [50]. Hence, the *Schottky* barrier height ($\Delta\varphi(0)$), which can be used as a measure of the depletion of oxide-ion vacancies at the space-charge layers and was calculated by

$$\frac{\sigma_{bulk}}{\sigma^*_{g.b}} = \frac{\exp\left(2 \times \frac{e\Delta\varphi(0)}{k_B \cdot T}\right)}{4 \times \frac{e\Delta\varphi(0)}{k_B \cdot T}} \tag{11}$$

where e is the electron charge, and k_B and T have the usual meanings. Figure 10 a shows a lower $\frac{\sigma_{bulk}}{\sigma^*_{g.b.}}$ ratio for the CGO20 composition, leading it to exhibit the lower $\Delta\varphi(0)$ values in Fig. 10b. The observation of a lower barrier height in CGO materials with increased Gd-content has traditionally been related to an increased segregation of Gd'_{Ce} species to the grain boundaries at higher doping contents, where their presence can attenuate the depletion of oxide-ion vacancies near the grain boundary core [49], producing an improvement in the specific grain boundary conductivity.

In contrast, such a suggestion fails to provide a rational explanation for the current results, where both intrinsic terms of the grain boundary ($\sigma^*_{g.b.}$ and $f_{g.b.}$) are noted to be similar, Fig. 9. A possible justification for this divergence could be related to the relatively low sintering temperature used in the present work (1350 °C). Standard, higher sintering temperature routes, e.g., (1600 °C) [50], most likely

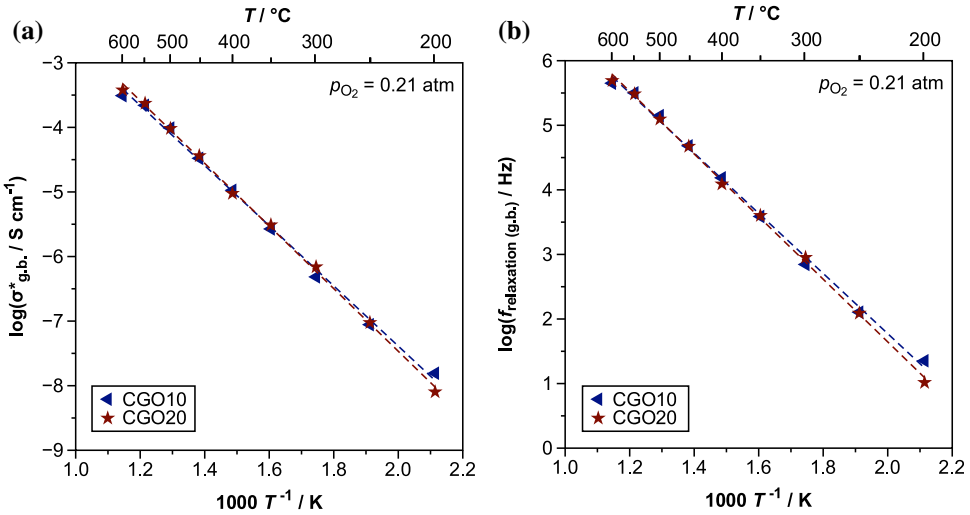

Figure 9 Temperature dependence of: **a** specific grain boundary conductivity; **b** grain boundary relaxation frequency. Data obtained for CGO10 and CGO20 in air in the temperature range 200–600 °C.

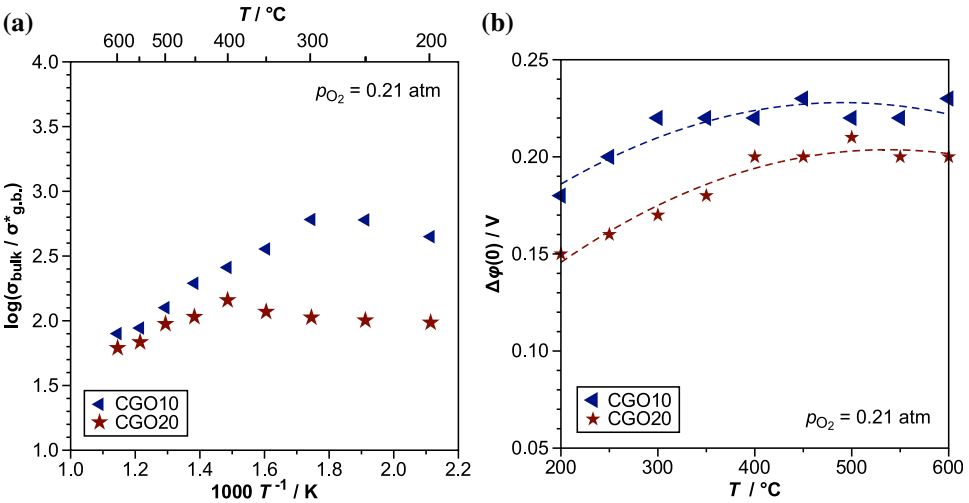

Figure 10 Temperature dependence of: **a** ratio between the bulk and specific grain boundary conductivity; **b** the *Schottky* barrier height. Data calculated for CGO10 and CGO20 in air, obtained in the temperature range 200–600 °C.

favor the segregation of $[Gd'_{Ce}]$ to the space-charge layers of the grain boundaries, as previously reported [54], while this is not possible at the lower sintering temperature (1350 °C) of the current work due to insufficient cation mobility. This feature is interesting and leads to both the CGO10 and CGO20 compositions offering similar total conductivity behaviors in the present proteic sol–gel route, in contrast to that of, higher temperature, literature preparation routes, where the CGO20 composition is commonly reported to offer slight electrical advantage [50, 55].

Conclusions

The proteic sol–gel method was successfully employed to synthesize CeO_2, CGO10 and CGO20 ceramics, leading to final dense ceramics with relative densities between 96 and 98% after sintering at the relatively low temperature of 1350 °C. These values are in line with previous reports using different processing routes, where higher sintering temperatures have needed to be employed. Microstructural analysis revealed significant differences in the grain sizes among the samples according to the dopant concentration, with lower grain sizes recorded for the Gd-doped ceria samples. The existence of defect associations was shown to have a strong negative impact on the bulk conductivity of the CGO20 ceramics, leaving the CGO10 material to be the peak performing bulk composition. In contrast, negligible differences were observed between the specific grain boundary conductivities recorded for both Gd-doped samples. This result deviates from that of CGO ceramics produced by traditional higher temperature preparation routes in the literature, and

was suggested to be related to the lower sintering temperatures used in the current route that may prevent segregation of the Gd-dopant to the grain boundary. The current article provides an attractive alternative route to produce highly dense Gd-doped ceramics at relatively lower sintering temperatures and with low-cost precursors. The herein adopted gelatin-based sol–gel synthesis is shown to be a suitable chemical approach to prepare functional materials for solid oxide electrochemical devices.

Acknowledgements

This study was financed in part by the Coordenação de Aperfeiçoamento de Pessoal de Nível Superior (CAPES/Brazil, Finance Code 001 and grant numbers 1762100 and 88882.344798/2019-01) and the Conselho Nacional de Desenvolvimento Científico e Tecnológico (CNPq/Brazil, reference number 200439/2019-7). Carlos A. Paskocimas thanks CNPq/Brazil (446126/2014-4, 308548/2014-0 and 307236/2018-8). Daniel A. Macedo acknowledges CNPq (Brazil, 431428/2018-2 and 309430/2019-4). The Aveiro team acknowledge projects POCI-01-0145-FEDER-032241, UID/EMS/00481/2019-FCT, CENTRO-01-0145-FEDER-022083, funded by FEDER, Centro Portugal Regional Operational Programme (Centro2020), under the PORTUGAL 2020 Partnership Agreement, through the European Regional Development Fund (ERDF) and by national funds (OE), through FCT/MCTES.

Electronic supplementary material: The online version of this article (https://doi.org/10.1007/s10853-020-05173-6) contains supplementary material, which is available to authorized users.

References

[1] Huijsmans JPP, van Berkel FPF, Christie GM (1998) Intermediate temperature SOFC—a promise for the 21st century. J Power Sources 71:107–110. https://doi.org/10.1016/S0378-7753(97)02789-4

[2] Nechache A, Cassir M, Ringuedé A (2014) Solid oxide electrolysis cell analysis by means of electrochemical impedance spectroscopy: a review. J Power Sources 258:164–181. https://doi.org/10.1016/j.jpowsour.2014.01.110

[3] Steele BCH, Heinzel A (2001) Materials for fuel-cell technologies. Nature 414:345–352. https://doi.org/10.1142/9789814317665_0031

[4] Dönmez G, Sarıboğa V, Gürkaynak Altinçekiç T, Öksüzömer MAF (2014) Polyol synthesis and investigation of $Ce_{1-x}RE_xO_{2-x/2}$ (RE = Sm, Gd, Nd, La, $0 \leq x \leq 0.25$) eElectrolytes for IT-SOFCs. J Am Ceram Soc 98:501–509. https://doi.org/10.1111/jace.13300

[5] Kharton VV, Marques FMB, Atkinson A (2004) Transport properties of solid oxide electrolyte ceramics: a brief review. Solid State Ionics 174:135–149. https://doi.org/10.1016/j.ssi.2004.06.015

[6] Zhou Y, Rahaman MN (1997) Effect of redox reaction on the sintering behavior of cerium oxide. Acta Mater 45:3635–3639. https://doi.org/10.1016/S1359-6454(97)00052-9

[7] Jadhav LD, Chourashiya MG, Subhedar KM et al (2009) Synthesis of nanocrystalline Gd doped ceria by combustion technique. J Alloys Compd 470:383–386. https://doi.org/10.1016/j.jallcom.2008.02.077

[8] Lima CGM, Santos TH, Grilo JPF et al (2015) Synthesis and properties of CuO-doped $Ce_{0.9}Gd_{0.1}O_{2-\delta}$ electrolytes for SOFCs. Ceram Int 41:4161–4168. https://doi.org/10.1016/j.ceramint.2014.12.093

[9] Fagg DP, Kharton VV, Frade JR (2002) P-type electronic transport in $Ce_{0.8}Gd_{0.2}O_{2-\delta}$: The effect of transition metal oxide sintering aids. J Electroceramics 9:199–207. https://doi.org/10.1023/A:1023269326651

[10] Grilo JPF, Macedo DA, Nascimento RM, Marques FMB (2019) Electronic conductivity in Gd-doped ceria with salt additions. Electrochim Acta 318:977–988. https://doi.org/10.1016/j.electacta.2019.06.148

[11] Loureiro FJA, Souza GS, Graça VCD et al (2019) Nickel-copper based anodes for solid oxide fuel cells running on hydrogen and biogas: Study using ceria-based electrolytes with electronic short-circuiting correction. J Power Sources 438:227041–227049. https://doi.org/10.1016/j.jpowsour.2019.227041

[12] Zarkov A, Stanulis A, Salkus T et al (2016) Synthesis of nanocrystalline gadolinium doped ceria via sol–gel combustion and sol–gel synthesis routes. Ceram Int 42:3972–3988. https://doi.org/10.1016/j.ceramint.2015.11.066

[13] Santos JRD, Loureiro FJA, Grilo JPF et al (2018) Understanding the cathodic polarisation behaviour of the misfit $[Ca_2CoO_{3-\delta}]_q[CoO_2]$ (C349) as oxygen electrode for IT-SOFC. Electrochim Acta 285:214–220. https://doi.org/10.1016/j.electacta.2018.08.018

[14] Emerenciano AA, Araújo AJM, Grilo JPF et al (2019) Environmentally friendly synthesis methods to obtain the misfit $[Ca_2CoO_{3-\delta}]_{0.62}[CoO_2]$ thermoelectric material. Mater Lett 254:286–289. https://doi.org/10.1016/j.matlet.2019.07.053

[15] Pechini MP (1967) Method of preparing lead and alkaline earth titanates and niobates and coating method using the same to form a capacitor. https://patents.google.com/patent/US3330697A/en

[16] Silva RM, Raimundo RA, Fernandes WV et al (2018) Proteic sol-gel synthesis, structure and magnetic properties of Ni/NiO core-shell powders. Ceram Int 44:6152–6156. https://doi.org/10.1016/j.ceramint.2017.12.248

[17] Cela B, Macedo DA, Souza GL et al (2011) NiO-CGO in situ nanocomposite attainment: One step synthesis. J Power Sources 196:2539–2544. https://doi.org/10.1016/j.jpowsour.2010.11.026

[18] Araujo AJM, Sousa ARO, Grilo JPF et al (2016) Preparation of one-step NiO/Ni-CGO composites using factorial design. Ceram Int 42:18166–18172. https://doi.org/10.1016/j.ceramint.2016.08.131

[19] Grilo JPF, Moura CG, Macedo DA et al (2017) Effect of composition on the structural development and electrical conductivity of NiO-GDC composites obtained by one-step synthesis. Ceram Int 43:8905–8911. https://doi.org/10.1016/j.ceramint.2017.04.027

[20] Silva TR, Silva VD, Ferreira LS et al (2020) Role of oxygen vacancies on the energy storage performance of battery-type NiO electrodes. Ceram Int 46:9233–9239. https://doi.org/10.1016/j.ceramint.2019.12.176

[21] Ferreira LS, Silva TR, Silva VD et al (2020) Proteic sol-gel synthesis, structure and battery-type behavior of Fe-based spinels (MFe_2O_4, M = Cu Co, Ni). Adv Powder Technol 31:604–613. https://doi.org/10.1016/j.apt.2019.11.015

[22] Lima CGM, Silva RM, de Aquino FM et al (2017) Proteic sol-gel synthesis of copper doped misfit Ca-cobaltites with potential SOFC application. Mater Chem Phys 187:177–182. https://doi.org/10.1016/j.matchemphys.2016.11.063

[23] Ferreira LS, Silva TR, Santos JRD et al (2019) Structure, magnetic behavior and OER activity of $CoFe_2O_4$ powders obtained using agar-agar from red seaweed (Rhodophyta). Mater Chem Phys 237:121847. https://doi.org/10.1016/j.matchemphys.2019.121847

[24] (2004) ISO 19318:2004, Surface chemical analysis—X-ray photoelectron spectroscopy—reporting of methods used for charge control and charge correction. https://www.iso.org/standard/33783.html

[25] (2015) ASTM E1523–15, Standard guide to charge control and charge referencing techniques in X-ray photoelectron spectroscopy. ASTM International, West Conshohocken, PA. www.astm.org

[26] Yeh JJ, Lindau I (1985) Atomic subshell photoionization cross sections and asymmetry parameters: $1 \leqslant Z \leqslant 103$. At Data Nucl Data Tables 32:1–155. https://doi.org/10.1016/0092-640X(85)90016-6

[27] Braga TP, Dias DF, de Sousa MF et al (2015) Synthesis of air stable FeCo alloy nanocrystallite by proteic sol-gel method using a rotary oven. J Alloys Compd 622:408–417. https://doi.org/10.1016/j.jallcom.2014.10.074

[28] Shannon RD (1976) Revised effective ionic radii and systematic studies of interatomic distances in halides and chalcogenides. Acta Crystallogr Sect A 32:751–767. https://doi.org/10.1107/S0567739476001551

[29] Rietveld HM (1969) A profile refinement method for nuclear and magnetic structures. J Appl Crystallogr 2:65–71. https://doi.org/10.1107/S0021889869006558

[30] Guo M, Lu J, Wu Y et al (2011) UV and visible Raman studies of oxygen vacancies in rare-earth-doped ceria. Langmuir 27:3872–3877. https://doi.org/10.1021/la200292f

[31] He D, Hao H, Chen D et al (2017) Synthesis and application of rare-earth elements (Gd, Sm, and Nd) doped ceria-based solid solutions for methyl mercaptan catalytic decomposition. Catal Today 281:559–565. https://doi.org/10.1016/j.cattod.2016.06.022

[32] Banerji A, Grover V, Sathe V et al (2009) CeO_2-Gd_2O_3 system: unraveling of microscopic features by Raman spectroscopy. Solid State Commun 149:1689–1692. https://doi.org/10.1016/j.ssc.2009.06.045

[33] Araújo AJM, Silva VD, Sousa ARO et al (2019) Battery-like behavior of Ni-ceria based systems: Synthesis, surface defects and electrochemical assessment. Ceram Int 45:7157–7165. https://doi.org/10.1016/j.ceramint.2018.12.222

[34] Upadhyaya DD, Bhat R, Ramanathan S et al (1994) Solute effect on grain growth in ceria ceramics. J Eur Ceram Soc 14:337–341. https://doi.org/10.1016/0955-2219(94)90070-1

[35] Inaba H, Nakajima T, Tagawa H (1998) Sintering behaviors of ceria and gadolinia-doped ceria. Solid State Ionics 106:263–268. https://doi.org/10.1016/s0167-2738(97)00496-7

[36] Peng R, Xia C, Peng D, Meng G (2004) Effect of powder preparation on $(CeO_2)_{0.8}(Sm_2O_3)_{0.1}$ thin film properties by screen-printing. Mater Lett 58:604–608. https://doi.org/10.1016/S0167-577X(03)00578-0

[37] Xia C, Liu M (2002) Microstructures, conductivities, and electrochemical properties of $Ce_{0.9}Gd_{0.1}O_2$ and GDC–Ni anodes for low-temperature SOFCs. Solid State Ionics 152–153:423–430. https://doi.org/10.1016/S0167-2738(02)00381-8

[38] Arabac A, Öksüzömer MF (2012) Preparation and characterization of 10 mol% Gd doped CeO_2 (GDC) electrolyte for SOFC applications. Ceram Int 38:6509–6515. https://doi.org/10.1016/j.ceramint.2012.05.030

[39] Tian R, Zhao F, Chen F, Xia C (2011) Sintering of Samarium-doped ceria powders prepared by a glycine-nitrate process. Solid State Ionics 192:580–583. https://doi.org/10.1016/j.ssi.2010.08.003

[40] Sındıraç C, Büyükaksoy A, Akkurt S (2019) Electrical properties of gadolinia doped ceria electrolytes fabricated by infiltration aided sintering. Solid State Ionics 340:115020. https://doi.org/10.1016/j.ssi.2019.115020

[41] Cheng J, Zha S, Fang X et al (2002) On the green density, sintering behavior and electrical property of tape cast $Ce_{0.9}Gd_{0.1}O_{1.95}$ electrolyte. Mater Res Bull 37:2437–2446. https://doi.org/10.1016/S0025-5408(02)00931-5

[42] Gondolini A, Mercadelli E, Sanson A et al (2011) Microwave-assisted synthesis of gadolinia-doped ceria powders for solid oxide fuel cells. Ceram Int 37:1423–1426. https://doi.org/10.1016/j.ceramint.2011.01.010

[43] Chen M, Zhang H, Fan L et al (2014) Ceria-carbonate composite for low temperature solid oxide fuel cell: Sintering aid and composite effect. Int J Hydrogen Energy 39:12309–12316. https://doi.org/10.1016/j.ijhydene.2014.04.004

[44] Fuentes RO, Baker RT (2008) Synthesis and properties of Gadolinium-doped ceria solid solutions for IT-SOFC electrolytes. Int J Hydrogen Energy 33:3480–3484. https://doi.org/10.1016/j.ijhydene.2007.10.026

[45] Suda E, Pacaud B, Mori M (2006) Sintering characteristics, electrical conductivity and thermal properties of La-doped ceria powders. J Alloys Compd 408–412:1161–1164. https://doi.org/10.1016/j.jallcom.2004.12.135

[46] Kang YJ, Choi GM (2009) The effect of alumina and Cu addition on the electrical properties and the SOFC performance of Gd-doped CeO_2 electrolyte. Solid State Ionics 180:886–890. https://doi.org/10.1016/j.ssi.2009.02.021

[47] Sánchez-Bautista C, Dos Santos-García AJ, Peña-Martínez J, Canales-Vázquez J (2010) Processing of samarium doped ceria for IT-SOFC. Grain boundary effect on the electrical conductivity. Bol la Soc Española Ceram y Vidr 49:7–14

[48] Santos TH, Grilo JPF, Loureiro FJA et al (2018) Structure, densification and electrical properties of Gd^{3+} and Cu^{2+} co-doped ceria solid electrolytes for SOFC applications: effects of Gd_2O_3 content. Ceram Int 44:2745–2751. https://doi.org/10.1016/j.ceramint.2017.11.009

[49] Guo X, Waser R (2006) Electrical properties of the grain boundaries of oxygen ion conductors: acceptor-doped zirconia and ceria. Prog Mater Sci 51:151–210. https://doi.org/10.1016/j.pmatsci.2005.07.001

[50] Pérez-Coll D, Núñez P, Ruiz-Morales JC et al (2007) Reexamination of bulk and grain boundary conductivities of $Ce_{1-x}Gd_xO_{2-\delta}$ ceramics. Electrochim Acta 52:2001–2008. https://doi.org/10.1016/j.electacta.2006.08.009

[51] Zhang TS, Ma J, Huang HT et al (2003) Effects of dopant concentration and aging on the electrical properties of Y-doped ceria electrolytes. Solid State Sci 5:1505–1511. https://doi.org/10.1016/j.solidstatesciences.2003.10.001

[52] Guo X, Maier J (2001) Grain boundary blocking effect in Zirconia: a Schottky barrier analysis. J Electrochem Soc 148:E121–E126. https://doi.org/10.1149/1.1348267

[53] Pérez-Coll D, Núñez P, Frade JR (2011) The role of SiO_2 and sintering temperature on the grain boundary properties of $Ce_{0.8}Sm_{0.2}O_{2-\delta}$. J Power Sources 196:8383–8390. https://doi.org/10.1016/j.jpowsour.2011.06.075

[54] Shirpour M, Rahmati B, Sigle W et al (2012) Dopant segregation and space charge effects in proton-conducting $BaZrO_3$ perovskites. J Phys Chem C 116:2453–2461. https://doi.org/10.1021/jp208213x

[55] Esposito V, Traversa E (2008) Design of electroceramics for solid oxides fuel cell applications: playing with Ceria. J Am Ceram Soc 91:1037–1051. https://doi.org/10.1111/j.1551-2916.2008.02347.x